This is a repository copy of *Forward models of torsional waves: dispersion and geometric effects*.

Version: Published Version

Article:

Forward models of torsional waves: dispersion and geometric effects

G. A. Cox, P. W. Livermore and J. E. Mound

School of Earth and Environment, University of Leeds, Leeds LS2 9JT, *UK. E-mail: eegac@leeds.ac.uk*

SUMMARY

Alfvén waves are a set of transverse waves that propagate in an electrically conducting fluid in the presence of an ambient magnetic field. Studies of such waves in the Earth's interior are important because they can be used to make inferences about the structure and physical properties of the core that would otherwise remain inaccessible. We produce 1-D forward models of cylindrical torsional Alfvén waves in the Earth's core, also known as torsional oscillations, and study their evolution in a full sphere and an equatorially symmetric spherical shell. Here, we find that travelling torsional waves undergo significant geometric dispersion that increases with successive reflections from the boundaries such that an initial wave pulse becomes unidentifiable within three transits of the core. Low amplitude wakes trail behind sharply defined pulses during propagation, a phenomenon that we interpret using the failure of Huygens' principle in even dimensions. We investigate the relationship between geometric dispersion and wavelength, concluding that long-wavelength features are more dispersive than short-wavelength features. This result is particularly important because torsional waves that have been inferred in the Earth's core from secular variation are relatively long wavelength, and are therefore likely to undergo significant dispersion within the core. When stress-free boundary conditions on angular velocity are applied, waves are reflected at the equator of the core–mantle boundary with the same sign as the incident wave. Waves that pass through the rotation axis undergo a pseudo-reflection and display a more complicated behaviour due to a phase shift. In an equatorially symmetric shell, we identify a weak reflection at the tangent cylinder due to geometric effects.

Key words: Numerical solutions; Dynamo: theories and simulations; Rapid time variations; Core, outer core and inner core; Planetary interiors.

1 INTRODUCTION

The geomagnetic field is continually generated and maintained against decay by convective motions in the fluid outer core through a process known as the geodynamo. Despite much scientific interest, a full understanding of the dynamics and evolution of the outer core remains elusive, partly because the Earth's deep interior cannot be observed directly. Theoretical considerations suggest that the geodynamo is in the strong field regime, in which the dominant force balance is magnetostrophic (e.g. Hollerbach 1996; Roberts 2007). This balance is between the Coriolis force, the pressure gradient, buoyancy forces and the Lorentz force, with viscous and inertial forces negligible such that

$$2\rho_0 \mathbf{\Omega} \times \boldsymbol{u} = -\nabla p + \rho' \boldsymbol{g} + \boldsymbol{J} \times \boldsymbol{B}, \qquad (1)$$

where ρ_0 is the hydrostatic reference density, $\mathbf{\Omega}$ is the angular velocity vector of the Earth, $\boldsymbol{u}$ is the fluid velocity, p is the non-hydrostatic contribution to pressure, ρ' is the departure from the hydrostatic reference density, $\boldsymbol{g}$ is the acceleration due to gravity, $\boldsymbol{J}$ is the electric current density and $\boldsymbol{B}$ is the magnetic field. The Coriolis force, arising due to the rotation of the Earth, plays a key role in determining the large-scale dynamics of the outer core because rapid rotation tends to prevent large variations in velocity parallel to the rotation axis (the Taylor–Proudman theorem). When the dominant force balance involves only the Coriolis force and the pressure gradient in spherical geometry, the flow is said to be geostrophic and the Taylor–Proudman theorem implies that the only permitted flow is purely zonal (i.e. in the azimuthal direction; Bullard & Gellman 1954). This constraint requires that core fluid moves in rigid cylinders, coaxial with the rotation axis, as shown in Figs 1(a) and 2.

Assuming an electrically insulating mantle, measurements of the geomagnetic field and its time variations may be downward continued to the core–mantle boundary (CMB) and inverted to construct maps of flow at the core surface (Backus 1968). Dynamical assumptions, such
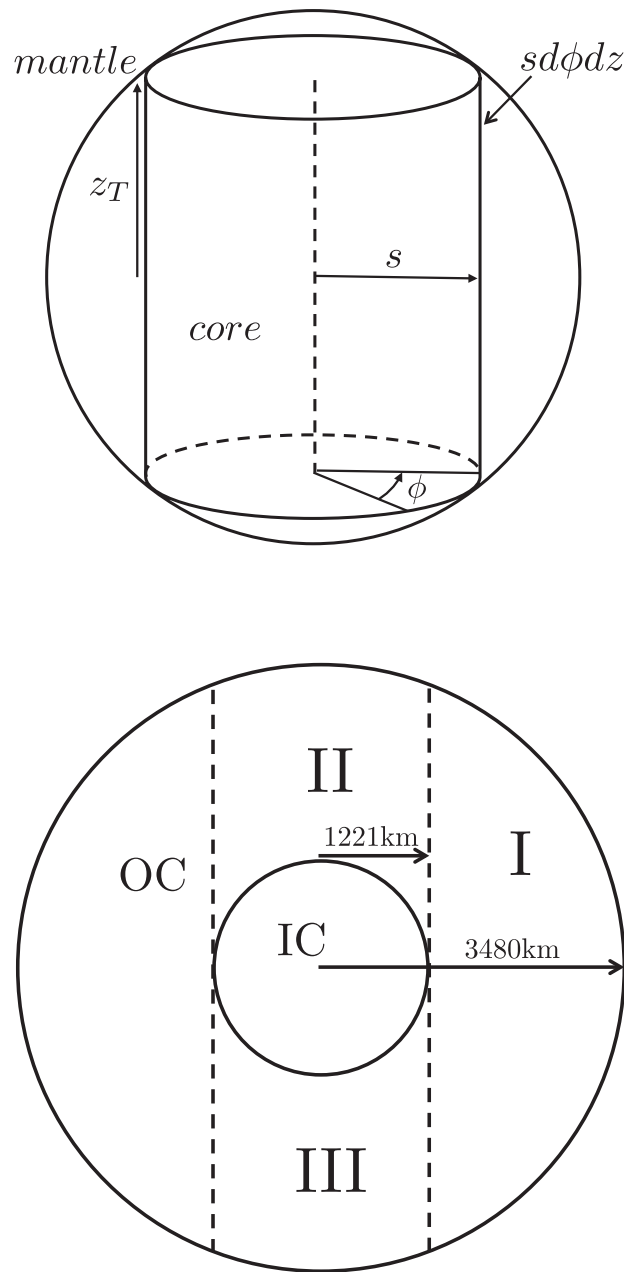
Figure 1. (a) Geometry of the geostrophic cylinders defined in a cylindrical coordinate system. The symbols s, ϕ and z describe, respectively, radial distance from the rotation axis, azimuth and height. The cylinder half height is denoted z_T. All of the fluid on the same cylindrical surface of radius s has the same velocity $u_\phi(s)$. After Dumberry (2009). (b) The Earth's core is divided into three coupled regions. (I) The region of the outer core (OC) that is outside the tangent cylinder. (II) The region of the outer core that lies inside the tangent cylinder and above the inner core (IC). (III) The region of the outer core that lies inside the tangent cylinder and below the inner core. The tangent cylinder is shown as a dashed line between region I and regions II and III.

as geostrophic time-dependent zonal motions, can be used to constrain the flow model. Due to its simple geometry and the presumed rigidity of geostrophic cylinders, this part of the flow field may then be extrapolated into the core's interior (Le Mouël 1984).

Taylor (1963) first showed that, in the magnetostrophic balance of eq. (1), the azimuthal Lorentz force must vanish when averaged over an arbitrary cylindrical surface that is coaxial with the rotation axis such that

$$\int_z \oint_\phi (\boldsymbol{J} \times \boldsymbol{B})_\phi s \, d\phi \, dz = 0, \tag{2}$$

where the coordinates (s, ϕ, z) are defined in a cylindrical geometry (Fig. 1a) and the subscript $()_\phi$ describes the azimuthal component of a vector. This imposes a condition on the morphology of the internal magnetic field and an associated dynamic state, which are called the Taylor constraint and Taylor state, respectively. Taylor's constraint specifies that the magnetic field inside the core must be organized in
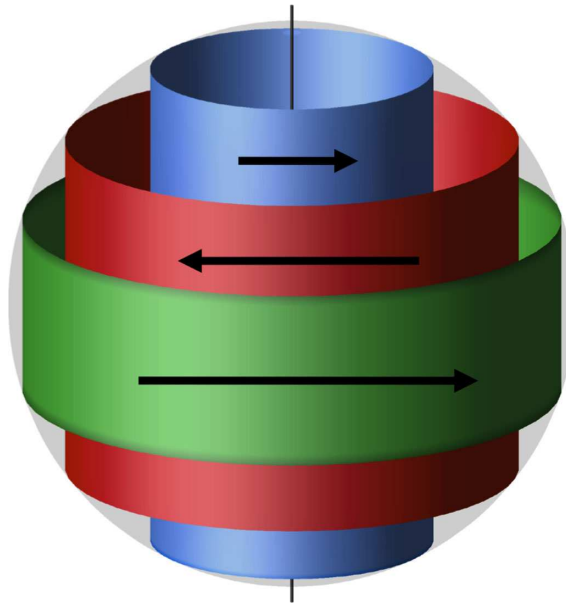
Figure 2. Torsional waves: azimuthal accelerations of rigid coaxial cylindrical surfaces. Each cylindrical surface moves with a different speed and is coupled to adjacent surfaces by the radial magnetic field B_s. Note that cylinder height decreases with increasing distance from the rotation axis.

such a way that the azimuthal Lorentz force vanishes on cylindrical surfaces. Taylor (1963) suggested that not only must the field obey this constraint at some initial time, but that departures from a Taylor state would excite azimuthal accelerations of these rigid cylindrical surfaces in order to reestablish the Taylor state at all later times. Relative rotation of adjacent cylinders perturbs magnetic field lines and the stretching of these field lines provides a restoring force to counter the perturbation. Fluid inertia carries the cylinder past the equilibrium position and the restoring force then changes direction, thus allowing torsional waves to propagate along radial magnetic field lines with a velocity that is linearly dependent on the intensity of the radial magnetic field. The observation of torsional waves in geophysical data would indicate that the Earth's core is in a quasi-Taylor state, in which the azimuthal Lorentz force vanishes when averaged over a cylinder, except for the part involved in torsional waves (Dumberry & Bloxham 2003).

Changes in core angular momentum can be calculated from core surface flow models. If the angular momentum of the core varies, there must be a corresponding variation in mantle angular momentum in order to satisfy the conservation law for this quantity. This leads to variations in length of day (ΔLOD). According to Jackson *et al.* (1993) and Jault *et al.* (1988), there is good correlation between changes in core angular momentum carried by geostrophic motions extracted from core flow models based on temporal changes in the geomagnetic field [secular variation (SV)], and observed changes in solid Earth angular momentum (ΔLOD) between 1920 and the present day. Braginsky (1970, 1984) first used torsional normal modes to explain observations of SV and decadal variations in ΔLOD. He made the link between theory and observations by deriving the torsional wave equation and predicted that torsional normal modes would have a period of approximately 60 yr if B_s, the cylindrical radial (s) component of the magnetic field is $\sim$0.2 mT.

More recently, several authors have reported observational evidence to support the existence of torsional waves in the core (Zatman & Bloxham 1997, 1999; Hide *et al.* 2000; Pais & Hulot 2000). Zatman & Bloxham (1997, 1999) concluded that the core flow model that best fits the observed axially and equatorially symmetric component of SV consists of a steady flow plus several damped harmonic waves with periods of decades. In both studies, they interpreted these waves as torsional normal modes and inverted them to derive an estimate of the internal magnetic field strength responsible for the waves and an estimate of core viscosity. Pais & Hulot (2000) used a method developed by Le Mouël *et al.* (1985) for determining the core surface flow accounting for the observed SV and obtained results in agreement with Zatman & Bloxham (1997, 1999). Hide *et al.* (2000) calculated the core angular momentum based on flow velocity models of Jackson *et al.* (1993), which were inferred from SV observed between 1840 and 1990. They noted a dominant latitude–dependent fluctuation with a 65-yr period, with angular momentum propagating from the equatorial to the polar regions.

However, recent work by Gillet *et al.* (2010) suggests that torsional waves are faster than previously concluded. They inverted the *gufm1* magnetic model (Jackson *et al.* 2000) for core flow and found that a recurring torsional wave matches the observed phase and amplitude of the observed 6-yr ΔLOD signal. As the propagation velocity of Alfvén waves is proportional to magnetic field strength, this would suggest that the internal core field strength is higher than previously assumed. Indeed, having calculated an ensemble of admissible profiles of torsional wave speed as a function of cylindrical radius, Gillet *et al.* (2010) inferred an internal field strength of 4 mT, compared to $\sim$2.5 mT calculated by Buffett (2010), $\sim$0.3 mT by Buffett *et al.* (2009) and $\sim$0.4 mT by Zatman & Bloxham (1997). Interestingly, not only does internal magnetic field strength differ from previous studies, but also the direction of propagation inferred by Gillet *et al.* (2010) is from the tangent cylinder

outwards, rather than from the equator to the poles as suggested by Hide *et al.* (2000). The tangent cylinder is the imaginary cylinder that is coaxial with the rotation axis and just touches the inner core (see Fig. 1b). In many previous studies, the direction of propagation had not been considered because standing oscillations were a better fit to the observed data than propagating waves. However, when Gillet *et al.* (2010) considered only the ΔLOD time-series filtered between 5 and 8 yr, they found that propagating waves best fit the data. Canet *et al.* (2009) derived a quasi-geostrophic model of rapid (SV timescales) core dynamics and used a variational data assimilation approach to link the model to the observed SV. Using both forward and adjoint models of torsional waves, which included both zonal and non-zonal velocity components, they concluded that torsional waves may be properly resolved using the last 10 yr of satellite measurements of the geomagnetic field. Buffett *et al.* (2009) used normal-mode analyses to recover the excitation source for torsional normal modes and identified the tangent cylinder as the main source region. A review of prior modelling attempts of torsional waves can be found in Jault & Légaut (2005).

Current knowledge of torsional waves based on geophysical observations is limited due to the sparsity of data, the non-uniqueness of core flow models and the fact that, apart from the geostrophic flow, internal core dynamics remain inaccessible. An advantage of investigating torsional waves using geodynamo simulations is that one can directly analyse the entire core flow field, examine force balances and look for Taylor states and/or torsional waves. Since the pioneering work of Glatzmaier & Roberts (1995), many numerical models of the geodynamo have been developed (for a detailed review, see Christensen & Wicht 2007). However, although geodynamo models are able to replicate some of the most important geomagnetic field features, such as polarity reversals, the simulations cannot run in the appropriate parameter regime for the Earth's core due to computational limitations. An important consequence of this is that the force balances involved in the models may differ from those expected in the Earth's core, which could prevent the excitation of torsional waves. In particular, even the most sophisticated geodynamo models operate with viscosities that are many orders of magnitude higher than estimated core values. If any waves were to develop in models with these high viscosities, they would be damped more quickly than expected in the Earth's core, which means that torsional waves do not have the same importance in numerical models as in the core.

Nevertheless, several authors have reported evidence of torsional waves and/or quasi-Taylor states in geodynamo models (Kuang 1999; Rotvig & Jones 2002; Stellmach & Hansen 2004; Takahashi *et al.* 2005; Wicht & Christensen 2010). Kuang (1999) investigated the force balance in the Kuang–Bloxham dynamo model (Kuang & Bloxham 1997) and concluded that torsional waves would develop in the model, and would be slightly damped by viscous dissipation. Dumberry & Bloxham (2003) obtained similar results using the same model and model parameters. They observed rigid azimuthal accelerations when examining the torque balance on cylindrical surfaces, but concluded that they were not conventional torsional waves because Reynolds stresses, which are usually neglected, were relatively large and played a major role in wave dynamics by providing an alternative means of balancing the azimuthal Lorentz force. Wicht & Christensen (2010) provide a more detailed review of the above work and other attempts to identify Taylor states and torsional waves in numerical simulations. They also present the results of a suite of geodynamo simulations performed at different parameters with the aim of identifying torsional waves based on two criteria; first, the presence of wave-like structures propagating with the expected Alfvén velocity and secondly, a dominant azimuthal Lorentz force during propagation. They found wave-like propagating structures in some models and were therefore able to confirm the predicted link between the magnetostrophic force balance, Taylor states and the existence of torsional waves. Recent work by Teed *et al.* (2013) also focused upon torsional waves in geodynamo simulations. Having performed 3-D simulations in a spherical shell in parameter regimes where Earth-like magnetic fields were produced, they identified torsional waves propagating at the theoretically predicted Alfvén speed in many of their simulations. Waves propagated in the cylindrical radial direction, either inwards or outwards, and were sometimes excited at the tangent cylinder. Typical core transit times were between 4 and 6 yr. Teed *et al.* (2013) noted that the frequency, location and direction of propagation of the waves were influenced by the choice of model parameters and also that excitation mechanisms for torsional waves were available throughout the outer core in their models. They calculated the driving terms for the observed torsional waves and concluded that both the Reynolds force and ageostrophic convection acting through the Lorentz force were important driving mechanisms.

Having briefly reviewed some of the previous work on torsional waves, from both a theoretical and observational point of view, it is evident that there remain many open questions with regard to the excitation and propagation of these waves in the outer core. These include the excitation mechanism of torsional waves, their direction of propagation, their period, their damping mechanisms and how these relate to core–mantle coupling and outer core properties. As previously discussed, Hide *et al.* (2000) suggested that torsional waves travel inwards from the equator to the poles, while Gillet *et al.* (2010) concluded that they propagate in the opposite direction, from the tangent cylinder to the equator. Since the torsional wave equation (discussed in Section 2) is time reversible, there is physically no preferred direction of propagation and one might expect to see torsional waves travelling in both directions. If, however, torsional waves were observed in geophysical data travelling in only one direction, this would provide information about their damping mechanisms, their reflections at boundaries and how and where the waves are excited within the core. Several excitation mechanisms for torsional waves have been proposed, which include deviations from a Taylor state (Taylor 1963), shear and violation of constraints at the tangent cylinder (Livermore & Hollerbach 2012; Livermore *et al.* 2013), solar cycles (Légaut 2005) and magnetic field gradients at the CMB (Braginsky 1984).

This work takes a different approach from many previous studies of torsional waves, which have primarily focused upon inverse modelling and geodynamo simulations. We use a 1-D forward modelling approach, rather than normal-mode computations, to evolve an initial wave pulse through time and investigate the effects of core geometry on torsional wave propagation. In particular, we examine local wave properties, boundary effects and geometric dispersion in a full sphere and in an equatorially symmetric spherical shell. The remainder of this paper is structured as follows: Section 2 describes the numerical methods and boundary conditions used in the forward models and Section 3 presents the modelling results. Discussion and conclusions follow in Section 4.

2 METHOD

When the magnetic field does not precisely satisfy Taylor's constraint, inertia may be reintroduced into eq. (2) and used to balance the azimuthal Lorentz force to obtain

$$\rho_0 \int_z \oint_\phi \frac{\partial u_\phi}{\partial t} s \, d\phi \, dz = \int_z \oint_\phi (\boldsymbol{J} \times \boldsymbol{B})_\phi s \, d\phi \, dz, \tag{3}$$

for an incompressible fluid. Since we have integrated in the ϕ and z directions, the problem collapses to one dimension and the above eq. (3), along with the induction equation, may be used to derive an equation for the cylindrical average of the geostrophic flow u_ϕ (see Braginsky 1970; Jault & Légaut 2005; Roberts & Aurnou 2011). The simplest form of the 1-D torsional wave equation is

$$\frac{\partial^2 u_\phi}{\partial t^2} = \frac{1}{s^2 \mu_0 \rho_0 z_T} \frac{\partial}{\partial s}\left[s^3 z_T \{B_s^2\} \frac{\partial\left(\frac{u_\phi}{s}\right)}{\partial s} \right], \tag{4}$$

where μ_0 is the permeability of free space, ρ_0 is the reference density (taken as $9900 \, \text{kg m}^{-3}$), z_T is the half-height of the geostrophic cylinder (a function of s in a spherical core) and $\{B_s^2\}$ is the square of the s-component of the magnetic field averaged over a geostrophic cylinder surface. The above equation does not include viscosity or dissipation terms that take into account coupling between the core and the mantle or between the inner core and the outer core. Neglecting the effects of a conducting layer at the base of the mantle and Ohmic and viscous dissipation allows us to isolate effects of core geometry and investigate their importance on torsional wave propagation.

Introducing an auxiliary variable, τ, we separate the second-order torsional wave eq. (4) into two first-order differential equations as follows:

$$\frac{\partial u_\phi}{\partial t} = \frac{1}{\mu_0 \rho_0 z_T s^2} \frac{\partial \tau}{\partial s}, \tag{5}$$

$$\frac{\partial \tau}{\partial t} = s^3 z_T \{B_s^2\} \frac{\partial\left(\frac{u_\phi}{s}\right)}{\partial s}. \tag{6}$$

Eqs (5) and (6) are solved, respectively, for u_ϕ and τ on separate staggered equally spaced grids using the third-order Adams Bashforth (AB3) method. The scheme is third order in time $\mathcal{O}[(\Delta t)^3]$ and second order in space $\mathcal{O}(h^2)$. The time step Δt and the grid spacing h were chosen such that all models were converged. The AB3 method requires knowledge of the solution at three previous time steps in order to calculate the next solution. The sequence of iterations is started with an initial profile for each variable at time $t = 0$, an explicit first-order Euler step at time $t = \Delta t$ and a second-order Adams Bashforth step at time $t = 2\Delta t$.

The analytic solutions to the torsional wave equation are known when (4) is solved in a cylinder (z_T is constant, Mound & Buffett 2007). The above Adams Bashforth method has been benchmarked against an independent normal-mode projection of these known solutions in cylindrical geometry and against a second-order leapfrog (LF) finite difference scheme. Although the solutions using the LF and AB3 method match closely, the AB3 method was chosen due to its strong damping of numerical instabilities. Unlike the LF method, it is not subject to time-splitting instability and has significantly smaller associated phase speed errors (Durran 1991).

Two codes were developed to solve the torsional wave equation in:

(i) a full sphere (no inner core). The cylinder height decreases with increasing cylindrical radius such that $z_T = \sqrt{r_c^2 - s^2}$, where r_c is the radius of the outer core (3480 km).

(ii) an equatorially symmetric spherical shell (the velocities u_ϕ are identical in regions II and III in Fig. 1b). Outside the tangent cylinder, the cylinder height is the same as in the full sphere case. Inside the tangent cylinder, the height of the inner core is subtracted from the full sphere case, which gives a piecewise differentiable function for cylinder height

$$z_T = \begin{cases} \sqrt{r_c^2 - s^2} - \sqrt{r_i^2 - s^2} & \text{if } s < r_i, \\ \sqrt{r_c^2 - s^2} & \text{if } s \geq r_i, \end{cases} \tag{7}$$

where r_i is the inner core radius (1221 km). The difference between the two models is purely geometric; there is no coupling mechanism between the inner and outer cores. Note that the height of the geostrophic cylinders tends to zero at the equator of the CMB ($s = r_c$).

The numerical scheme requires that both u_ϕ and τ are defined on their respective spatial grids at time $t = 0$ and that boundary conditions are imposed on u_ϕ at $s = 0$ and $s = r_c$. Despite the need for a boundary condition at $s = 0$, the rotation axis is not a physical boundary, but a singular point of the cylindrical coordinate system. Care must be taken that the physical solution, itself regular at $s = 0$, is not subject to such singularities. Lewis & Bellan (1990) detail the mathematical constraints that impose regularity on the solution at the origin in cylindrical coordinates. They state that the general form for the ϕ-component of any axisymmetric vector, $\boldsymbol{u}$, in cylindrical coordinates is

$$u_\phi = s f(s^2), \tag{8}$$

where f is any smooth function of s^2. The Taylor expansion of (8) includes only odd powers of s

$$u_\phi = a_0 s + a_1 s^3 + a_2 s^5 + ..., \tag{9}$$

from which it follows that $u_\phi = 0$ at the rotation axis. Dividing eq. (8) by s and differentiating with respect to s yields

$$\frac{\partial \left(\frac{u_\phi}{s}\right)}{\partial s}\Bigg|_{s=0} = 2sf'(s^2) = 0. \tag{10}$$

This means that the solution must satisfy constraints simultaneously imposed on both the velocity u_ϕ and $\frac{\partial \left(\frac{u_\phi}{s}\right)}{\partial s}$ at the rotation axis in cylindrical coordinates. Further differentiation of eq. (10) would yield an infinite hierarchy of higher order conditions that must also be satisfied at $s = 0$. Numerically, we impose only the regularity condition $u_\phi = 0$ at $s = 0$ in our models; all other necessary conditions are automatically satisfied. Note that in the following discussion we refer to interactions with, and reflections at, the 'boundaries' at $s = 0$ and $s = r_c$. The reader should regard these 'reflections' at the rotation axis as pseudo-reflections, because that they occur at a singular point of the coordinate system and not at a physical boundary.

Following Jault & Légaut (2005), we impose a stress-free boundary condition on the angular speed $\omega_g = u_\phi/s$ at the equator of the CMB ($s = r_c$)

$$\frac{\partial \omega_g}{\partial s}\Bigg|_{s=r_c} = 0. \tag{11}$$

Stress-free boundary conditions ensure that total angular momentum is conserved (see below). A Gaussian-like initial profile, that is not a normal-mode solution to the torsional wave equation but satisfies the boundary and regularity conditions, is chosen for u_ϕ. Although the choice of initial profile is somewhat arbitrary, the Gaussian-like profile has several desirable properties; it is smooth, continuous and infinitely differentiable. Also, its simple shape allows the investigation of how the form of the pulse changes during the wave evolution. The initial profile is given by

$$u_\phi = As^2(s - r_c)^2 e^{-\left(\frac{s-r_c/2}{\sigma}\right)^2}, \tag{12}$$

where A is a constant chosen such that the maximum value of the profile is 1 and σ determines the width of the pulse. Theory predicts that with stress-free boundary conditions applied at the equator of the CMB, total angular momentum of the core should be conserved. The total angular momentum, M_T of the waves is the integral of the angular momentum density over the whole core

$$M_T = \int_0^{r_c} u_\phi s^2 z_T \, ds. \tag{13}$$

From the definition of $\frac{\partial u_\phi}{\partial t}$ given by eq. (5), it follows that

$$\frac{\partial M_T}{\partial t} = \frac{1}{\mu_0 \rho_0} \int_0^{r_c} \frac{\partial \tau}{\partial s} \, ds = \frac{1}{\mu_0 \rho_0} [\tau]_0^{r_c}. \tag{14}$$

This integral vanishes if $\tau|_{s=r_c} = \tau|_{s=0}$ throughout wave evolution, which is guaranteed by the stress-free boundary condition at $s = r_c$ applied in eq. (6) and, following Canet *et al.* (2009), by initially setting the variable τ to zero on the whole domain.

For the majority of this work, we consider two models with a constant $\{B_s^2\}$ profile, one in a full sphere (model i) and the other in an equatorially symmetric spherical shell (model ii). In these models, the $\{B_s^2\}$ profile remains at a constant value of 4 (mT)^2. This value was chosen because it gives a core transit time of approximately 6 yr, which is consistent with the work of Gillet *et al.* (2010). We now non-dimensionalize the magnetic field and length scale, respectively, by 1 mT and the radius of the core. We leave the structure of the radial magnetic field B_s unspecified, except to remark that a constant $\{B_s^2\}$ profile requires a non-axisymmetric magnetic field at $s = 0$. Potential effects of variable $\{B_s^2\}$ are considered in a third model (model iii), which is in a full sphere geometry. Model (iii) uses the magnetic field profile shown in Fig. 13 in Section 3.3, which is based on a profile taken from a geodynamo simulation (Rob Teed, personal communication, 2013).

3 RESULTS

In this section, we present results obtained from our forward models of torsional waves. Figs 3–12 show results related to velocity u_ϕ, angular momentum and dispersion for the three wave models described in the previous section. The torsional wave equation does not define a magnitude for the velocity u_ϕ because it is linear and homogeneous, so the velocity in the following plots is scaled by the amplitude of the initial pulse, which is given by eq. (12).

3.1 Core geometry and wave propagation

The initial velocity profile, using $\sigma = 0.1$, in the models is smooth and has one positive peak at the midpoint of the domain ($s = r_c/2$). Fig. 3 shows the evolution of this pulse in the full sphere case, model (i). The first observation is that the initial waves are apparently non-dispersive and travel as distinct independent pulses before they first encounter the boundaries (0–3 yr). The initial pulse splits into two smaller positive peaks, one of which travels outwards towards the equator (a') and the other travels inwards towards the rotation axis (a). After approximately 3 yr, both pulses arrive at their respective boundaries and then reflect. When (a') reaches the equator of the CMB, it reflects with no change of sign such that (b') is also positive. A strong positive pulse (a) followed by a very weak negative pulse (b) converges on the rotation axis,
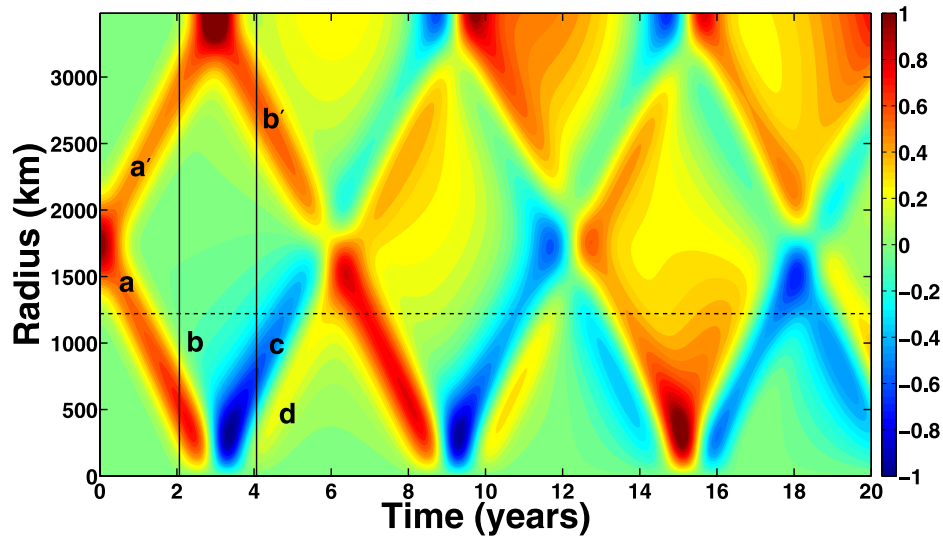
Figure 3. Contour plot of the velocity u_ϕ of torsional waves in a full sphere, with time on the horizontal axis and cylindrical radius on the vertical axis. Red corresponds to positive velocity and blue corresponds to negative velocity. The horizontal black dashed line represents the location of the tangent cylinder at $s = 1221$ km to aid comparison with the spherical shell case in Fig. 5. The two vertical lines show the times at which profiles are shown in Figs 8 and 9 (1 yr before and 1 yr after the waves reflect from the boundaries).
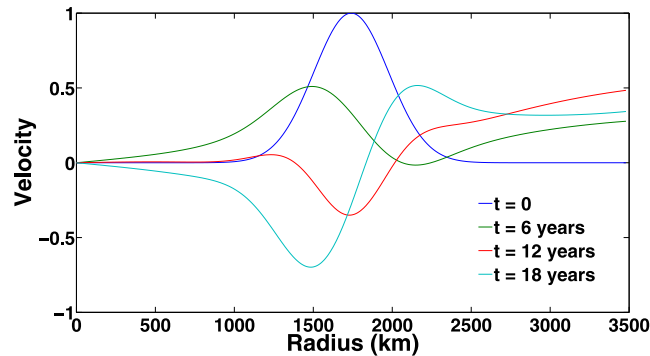

Figure 4. Velocity profiles of the waves at the start of evolution (blue), after one core transit (green), after two core transits (red) and after three core transits (cyan) in a full sphere.

and the returning wave train consists of a strong trough (*c*) followed by a small peak (*d*). Having reflected from the boundaries, the two wave trains (*b'*) and (*c*, *d*) traverse the core radius, meeting and interfering with each other after a further 3 yr. The waves continue to reflect from the boundaries and interfere, each time taking approximately 6 yr to traverse the entire core. Note that after one core transit time (6 yr), some of the wave energy has spread throughout the domain and the wave no longer travels entirely as distinct pulses. An evolving wave packet shape through time would indicate that some form of dispersion is occurring. It seems that successive reflections at the boundaries increase the effects of this dispersion such that after three core transit times most of the energy has spread out and the wave bears little resemblance to the initial velocity profile (Fig. 4).

　　The wave evolution in an equatorially symmetric spherical shell, Fig. 5, is very similar to that of a full sphere. Again, the initial wave pulse splits into an outwards travelling peak (*a'*) and an inwards travelling peak (*a*). Pulse (*a'*) hits the equator of the CMB after 3 yr and reflects with no change of sign. The positive pulse (*a*), followed by the weak negative pulse (*b*), reflects at the rotation axis to form a strong trough (*c*) and a small peak (*d*). These waves meet (*b'*) at approximately $t = 6$ yr and interfere. As in the spherical case, waves have a core transit time of approximately 6 yr and the pulses become more dispersed with increasing time.

　　An important observation is that the wave amplitude changes throughout propagation. In both geometries, peaks (*a*) and (*a'*) are not symmetric about $s = r_c/2$; the inwards travelling pulse (*a*) has a higher amplitude than the outwards travelling (*a'*) when traversing the central regions of the domain (Figs 3 and 5). At the rotation axis, the amplitude of pulse (*a*) drops to zero due to the regularity condition, while the wave amplitude of pulse (*a'*) is high in the region adjacent to the equator of the CMB. Jault & Légaut (2005) used geometric considerations to explain these variations of wave amplitude during torsional wave propagation through the core.

　　Fig. 6 shows the transport of angular momentum density $u_\phi s^2 z_T$ through the core for the full sphere model discussed earlier. The plot of angular momentum density is similar to the contour plot of velocity shown in Fig. 3, in that the initial pulse is shown splitting apart into two pulses travelling in opposite directions and these pulses are subsequently shown reflecting from the domain boundaries. The amplitude
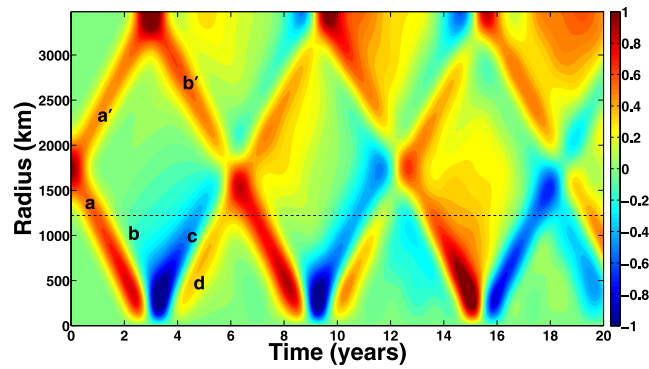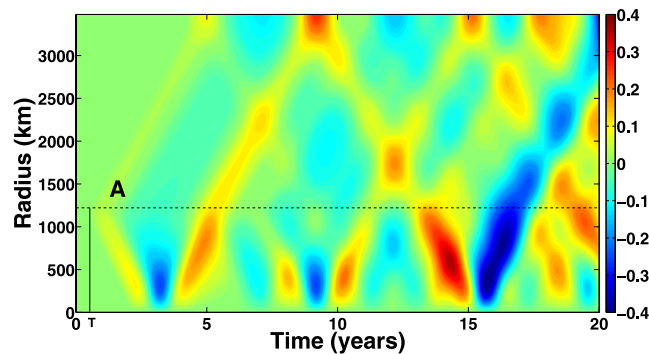
Figure 5. Contour plot of the velocity u_ϕ of torsional waves in an equatorially symmetric spherical shell, with time on the horizontal axis and cylindrical radius on the vertical axis. Red corresponds to positive velocity and blue corresponds to negative velocity. The horizontal black dashed line represents the location of the tangent cylinder at $s = 1221$ km.
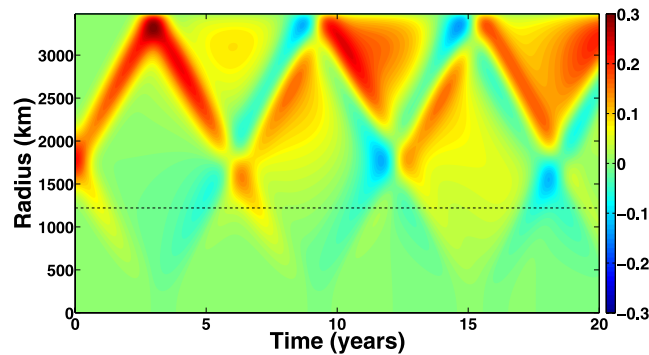
Figure 6. Contour plot of the angular momentum density $u_\phi s^2 z_T$ of torsional waves in a full sphere, with time on the horizontal axis and cylindrical radius on the vertical axis. Red corresponds to positive angular momentum density and blue corresponds to negative angular momentum density. The horizontal black dashed line represents the location of the tangent cylinder at $s = 1221$ km.

of angular momentum density is low in the region close to the rotation axis due to the influence of the s^2 contribution to angular momentum density, which decreases with decreasing cylindrical radius more rapidly than u_ϕ increases.

An interesting feature is observed in both the velocity and angular momentum density contour plots; after the initial pulse has separated, there remains a low-amplitude tail connecting the two pulses in the centre of the domain. This central region never returns to its initial quiescent state after the passage of the torsional waves as one might expect, but the wave fronts leave a low-amplitude negative trailing wake [labelled as pulse (*b*) in Figs 3 and 5]. In the case of the general wave equation for a scalar field, the failure of Huygens' principle in even spatial dimensions gives rise to trailing wakes behind sharply defined wave pulses [Courant & Hilbert (1962, pp. 765–766); Hadamard (1923, pp. 53, 176–177)]. Since torsional waves are symmetric 2-D waves due to their convergence on an axis at $s = 0$, we interpret the observed trailing wakes in terms of Huygens' principle in Section 4.1.

Figure 7. Contour plot of the difference in velocity u_ϕ when full sphere velocities were subtracted from the spherical shell case. Time is on the horizontal axis and cylindrical radius is on the vertical axis. Red corresponds to positive velocity differences and blue corresponds to negative velocity differences. The horizontal black dashed line represents the location of the tangent cylinder at $s = 1221$ km. Note the weak positive reflection (in yellow) from the tangent cylinder at time T~0.6 yr.
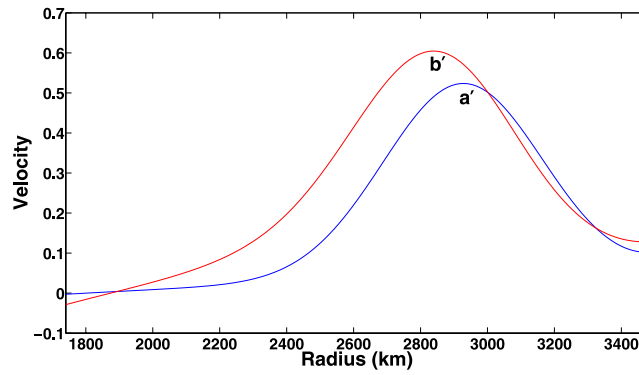
Figure 8. Velocity profiles of the waves 1 yr before (blue) and after (red) reflection at the equator of the core–mantle boundary ($s = r_c$) in a full sphere. The annotations correspond to those in Fig. 3 and the times at which the profiles were taken are shown in that figure as two vertical black lines.
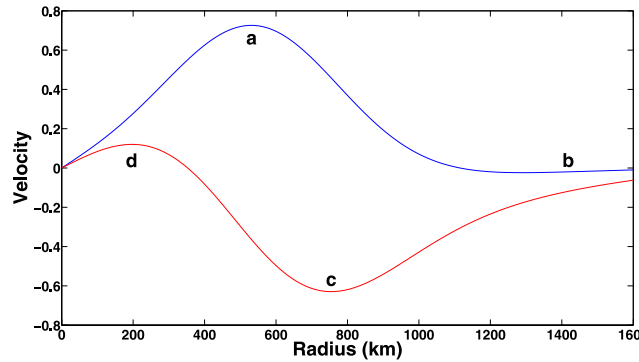

Figure 9. Velocity profiles of the waves 1 yr before (blue) and after (red) reflection at the rotation axis in a full sphere. The annotations correspond to those in Fig. 3 and the times at which the profiles were taken are shown in that figure as two vertical black lines.

Though theoretically predicted, numerically exact conservation of angular momentum in models is unlikely due to computational error. The total angular momentum of the initial wave pulse was compared to the total angular momentum of the wave profiles at every time step and we find that this quantity is conserved to a few parts in 10^4 for the models presented in this paper. Angular momentum is better conserved in models with better spatial resolution, which indicates that the spatial discretization is largely responsible for the observed small fluctuations of angular momentum.

Although Figs 3 and 5 appear quite similar, subtracting the full sphere velocities from the spherical shell velocities highlights some important differences between models (i) and (ii) (Fig. 7). The first of these differences is a weak reflection at the tangent cylinder. After the initial pulse splits apart and pulse (*a*) hits the tangent cylinder, a very weak reflection of the same sign (*A*) can be seen travelling away from the inner core after time T∼0.6 yr. Pulse (*A*) is much weaker than the incident pulse (*a*), with a reflection coefficient of approximately 0.07. The second difference between the two models is that the wave amplitude is higher near the rotation axis in the equatorially symmetric spherical shell model than in the full sphere model (pulses *a*, *b*, *c* and *d* in Figs 3 and 5, and the waves inside the tangent cylinder in Fig. 7). The amplitudes of the velocity differences between models (i) and (ii) increases with increasing time in Fig. 7. This could be due to the
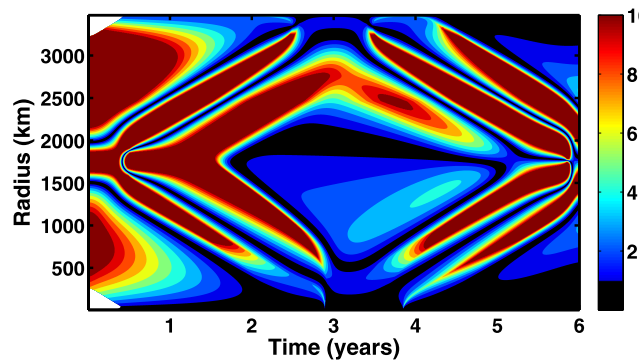
Figure 10. Contour plots of α, as defined by eq. (18), over one complete transit time (6 yr) in the full sphere model. Black regions ($\alpha < 1$) are locally 'dispersive', since term 1 is smaller than at least one of the other terms. Coloured regions are locally 'non-dispersive', with the magnitude of term 1 at least equal to that of the other terms in the blue regions and exceeding the other terms by at least a factor of 10 in the red regions. White regions show areas where the terms are very small and calculating the ratio would therefore be numerically intractable.
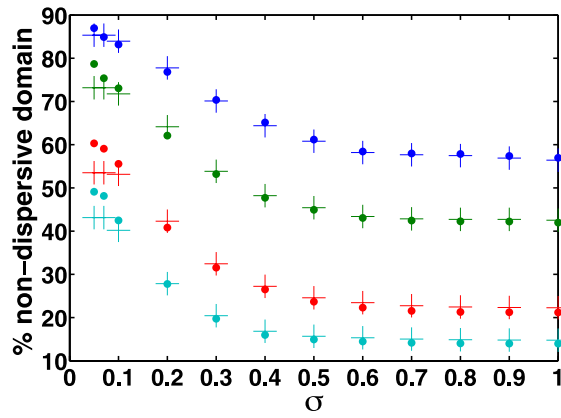
Figure 11. The percentage of the domain that is non-dispersive over one core transit time (6 yr) in the full sphere (crosses) and shell (circles) geometries according to the four different thresholds on α: 1 (blue), 2 (green), 5 (red) and 10 (cyan) as a function of initial pulse width. Lower σ values correspond to narrower initial velocity profiles.
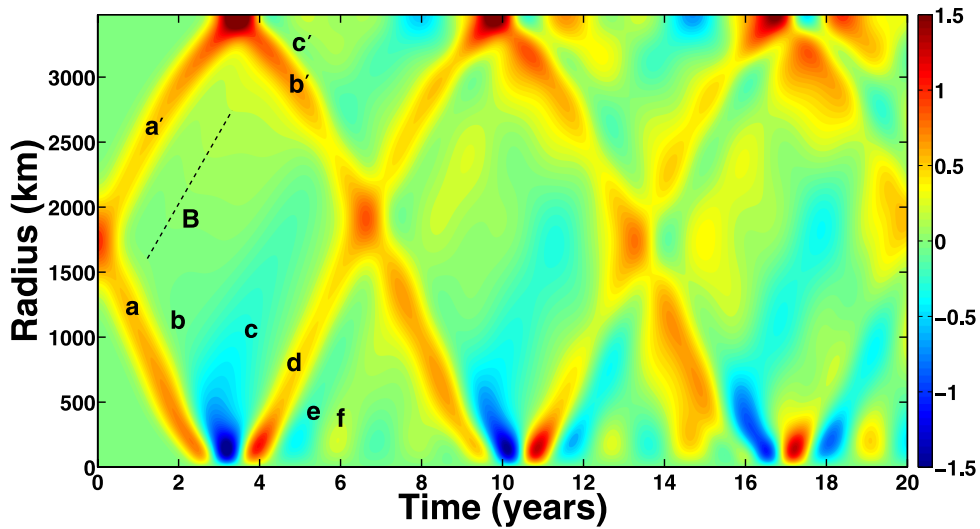
Figure 12. Contour plot of the velocity u_ϕ of torsional waves in a full sphere with the steady background magnetic field shown in Fig. 13, with time on the horizontal axis and cylindrical radius on the vertical axis. Red corresponds to positive velocity and blue corresponds to negative velocity. Pulse B, whose trajectory is plotted as a black dotted line, is an internal reflection from the global maximum of the magnetic field.

successive reflections from the tangent cylinder that only occur in the spherical shell model. Alternatively, since it appears that the waves in both models are subject to dispersion, the increasing amplitude with time in the difference plot in Fig. 7 may indicate that the phase difference between the models is increasing with time.

Figs 8 and 9 show the velocity profiles across the core 1 yr before and after the wave reflects from the boundaries in the full sphere geometry. Since we investigate the effects of core geometry on torsional waves, it is of interest to compare the boundary effects in the full sphere model results with those expected in the simplest possible geometry, which is 1-D Cartesian (wave on a string). In the latter case, after reflection at a stress-free boundary, the wave profiles at the same time before and after reflection, 1 yr for example, are identical. At a no-slip boundary, the wave changes sign and the reflected wave is the exact negative of the incoming wave. Since a stress-free boundary condition is applied at the equator of the CMB ($s = r_c$) in our torsional wave models, we might expect the incoming and reflected torsional wave profiles to match as they do in the Cartesian case. Although the incident (a') and reflected (b') wave profiles in Fig. 8 are of the same sign, the incoming pulse is not exactly recovered after reflection. At the rotation axis (see Fig. 9), the reflected wave profile (c, d) contains both positive and negative components, and is very different from the incident profile (a, b).

3.2 Dispersion

In the archetypical 1-D Cartesian 'wave on a string' example, the second spatial derivative of the velocity u is the only term on the right-hand side (RHS) of the 1-D wave equation given by

$$\frac{\partial^2 u}{\partial t^2} = c^2 \frac{\partial^2 u}{\partial x^2}. \tag{15}$$

D'Alembert first proposed that the solution to the above eq. (15) takes the form of two superposed waves travelling in opposite directions with speed c such that

$$u(x, t) = F(x - ct) + G(x + ct), \tag{16}$$

where F and G are two arbitrary twice differentiable functions that are found from the initial and boundary conditions. $F(x - ct)$ represents a wave travelling in the positive x-direction, while $G(x + ct)$ represents a wave travelling in the negative x-direction. Since the speed c remains constant and does not depend on wavenumber, the waves are non-dispersive. In other geometries, such as the cylindrically symmetric 2-D setting that we consider in this paper, the relevant wave equation includes additional terms on the RHS and the 1-D Cartesian (non-dispersive) case is approached when the relative magnitudes of these extra terms are small. Assuming a constant magnetic field profile $\{B_s^2\}$ across the core, expanding the RHS of the torsional wave equation gives

$$\frac{\partial^2 u_\phi}{\partial t^2} = \frac{\{B_s^2\}}{\mu_0 \rho_0} \left(\underbrace{\frac{\partial^2 u_\phi}{\partial s^2}}_{1} + \underbrace{\frac{1}{s}\frac{\partial u_\phi}{\partial s}}_{2} - \underbrace{\frac{s}{z_T^2}\frac{\partial u_\phi}{\partial s}}_{3} + \underbrace{\frac{u_\phi}{z_T^2}}_{4} - \underbrace{\frac{u_\phi}{s^2}}_{5} \right). \tag{17}$$

One measure of the dispersive properties of the modelled torsional waves is the ratio of the magnitude of the second spatial derivative (term 1) to the maximum value of the magnitude of the other four terms (terms 2–5) on the RHS of eq. (17). We define a measure α such that

$$\alpha = \frac{\left| \frac{\partial^2 u_\phi}{\partial s^2} \right|}{\max \left(\left| \frac{1}{s}\frac{\partial u_\phi}{\partial s} \right|, \left| \frac{s}{z_T^2}\frac{\partial u_\phi}{\partial s} \right|, \left| \frac{u_\phi}{z_T^2} \right|, \left| \frac{u_\phi}{s^2} \right| \right)}. \tag{18}$$

If α is sufficiently large, waves become effectively non-dispersive. For the purposes of the following discussion of our torsional wave models, we label waves as locally 'non-dispersive' if term 1 exceeds the largest of the other terms ($\alpha \geq 1$). The ratio α may be evaluated at every point in space during the wave evolution to determine what percentage of the spatial domain is dispersive or non-dispersive over a particular time duration.

Fig. 10 is a contour plot of α over one complete transit time (6 yr) in the full sphere geometry. Black regions ($\alpha < 1$) are locally 'dispersive', since term 1 is smaller than at least one of the other terms. Coloured regions are locally 'non-dispersive' according to our definition, with the magnitude of term 1 at least equal to that of the other terms in the blue regions and exceeding the other terms by at least a factor of 10 in the red regions. White regions show areas where the terms are all very small and calculating the ratio would therefore be numerically intractable. We see that in our geometry, geometric factors begin to dominate the second spatial derivative near the boundaries, especially near to the rotation axis, though the dispersion condition is also violated in central areas of the domain, where trailing wakes are observed. Since the condition given by eq. (18) evaluates the extent to which the torsional wave equation itself is non-dispersive, rather than the solutions to the torsional wave equation, it is of interest to compare the predicted dispersive regions of the domain with the regions in which dispersion is seen in our model results. Comparing the contour plots of the first 6 yr of wave evolution in Fig. 3 with the elements in Fig. 10, we find that wave dispersion, which manifests as an evolving wave pulse shape through time, coincides with regions of the domain where the second spatial derivative is dominated by another term, as predicted. We performed the same analysis, in both a sphere and spherical shell, using several initial velocity profiles of differing widths for threshold values on α of 1, 2, 5 and 10. Fig. 11 shows the percentage of the domain that is non-dispersive over one core transit time as a function of the initial pulse width. It shows that narrower Gaussian-like pulses (lower σ values) undergo less dispersion than wider pulses in both the full sphere and shell models. The models presented in Figs 3 and 5 both used $\sigma = 0.1$. In the full sphere case, this corresponds to the domain being at most 84 per cent non-dispersive over one transit time (using a threshold on α of 1). The spherical shell model is at most 83 per cent non-dispersive over the same period, using a threshold on α of 1. Using the threshold value of 1 only ensures that the second derivative (term 1) is at least the same order of magnitude as the other terms, not that it is the dominant term of the RHS of the torsional wave equation. A more realistic condition would be that the second derivative must be at least an order of magnitude higher than the other terms to be considered the dominant term. Using this more stringent threshold value of 10, we find that the domains in models (i) and (ii) are, respectively, only 40 and 42 per cent non-dispersive over one core transit time.

3.3 Torsional wave propagation in a spatially varying magnetic field

Since the magnetic field in the Earth's core is expected to vary on large length scales, it is of interest to study torsional wave evolution in a spatially varying ambient magnetic field. Fig. 12 shows the first 20 yr of torsional wave evolution in the spatially varying ambient magnetic field shown in Fig. 13.

As in previous results for constant $\{B_s^2\}$ models, the initial profile splits into two waves travelling in opposite directions, with a low-amplitude tail connecting the two pulses in the centre of the domain. These pulses take just over 6 yr to traverse the entire core. Waves reflect from the stress-free boundary at $s = r_c$ with no change of sign and with a partial change of sign at the rotation axis. We observe that wave energy becomes increasingly dispersed through the core with increasing time and that the initial profile is never recovered. In order to quantify this dispersion, two terms must be added to eq. (17) to account for spatial variations of the $\{B_s^2\}$ profile. The fully expanded torsional wave
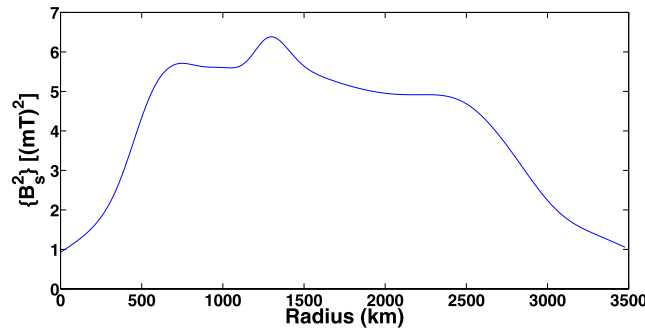
Figure 13. The spatially varying magnetic field, $\{B_s^2\}$, profile used in the full sphere model (iii).

equation now reads

$$\frac{\partial^2 u_\phi}{\partial t^2} = \frac{1}{\mu_0 \rho_0} \left[\{B_s^2\} \left(\underbrace{\frac{\partial^2 u_\phi}{\partial s^2}}_{1} + \underbrace{\frac{1}{s}\frac{\partial u_\phi}{\partial s}}_{2} - \underbrace{\frac{s}{z_T^2}\frac{\partial u_\phi}{\partial s}}_{3} + \underbrace{\frac{u_\phi}{z_T^2}}_{4} - \underbrace{\frac{u_\phi}{s^2}}_{5} \right) + \underbrace{\frac{\partial u_\phi}{\partial s}\frac{\partial \{B_s^2\}}{\partial s}}_{6} - \underbrace{\frac{u_\phi}{s}\frac{\partial \{B_s^2\}}{\partial s}}_{7} \right], \tag{19}$$

which suggests that the following ratio

$$\alpha = \frac{\{B_s^2\} \left| \frac{\partial^2 u_\phi}{\partial s^2} \right|}{\max \left(\left| \frac{\{B_s^2\}}{s}\frac{\partial u_\phi}{\partial s} \right|, \left| \frac{s\{B_s^2\}}{z_T^2}\frac{\partial u_\phi}{\partial s} \right|, \left| \frac{u_\phi \{B_s^2\}}{z_T^2} \right|, \left| \frac{u_\phi \{B_s^2\}}{s^2} \right|, \left| \frac{\partial u_\phi}{\partial s}\frac{\partial \{B_s^2\}}{\partial s} \right|, \left| \frac{u_\phi}{s}\frac{\partial \{B_s^2\}}{\partial s} \right| \right)} \tag{20}$$

should be evaluated at each point in space during wave evolution. We again use thresholds on α of 1, 2, 5 and 10, and find that over the first 6 yr of wave propagation, the domain is 88, 78, 55 and 36 per cent non-dispersive for these four thresholds. We note that these dispersion percentages are very similar to those obtained in the full sphere (i) and spherical shell (ii) models with constant $\{B_s^2\}$ profiles (see Fig. 11). Fig. 14 shows the regions of the domain that are labelled 'dispersive' (black) and 'non-dispersive' (coloured) for model (iii). As in previous models, we see that dispersion mainly occurs near to the rotation axis due to geometric factors and, to a lesser extent, in central parts of the domain where trailing wakes are observed.

Although we observe the same geometric features in all of the models, there are some important differences in wave behaviour between the variable field model (iii) and the constant field models (i) and (ii). First, the pulse trajectories in Fig. 12 are curved due to variations in the local Alfvén wave group velocity. Since the cylindrical average of the magnetic field $\{B_s^2\}$ varies across the core, and the local wave group speed depends on this quantity (see Section 3.4), the pulses accelerate when the magnetic field strength is increasing and decelerate when the magnetic field is weakening. One consequence of this is that pulses (a) and (a') do not reach their respective boundaries at the same time, and that waves (c, d) and (b') no longer intercept each other in the centre of the domain as in the constant $\{B_s^2\}$ profile models. The second observed feature is an internal reflection, labelled as pulse B in Fig. 12, which likely arises due to the relatively steep magnetic field gradient at $s = 1300\,\mathrm{km}$ (see the $\{B_s^2\}$ profile in Fig. 13). Thirdly, we observe several pulses of alternating polarity near to both the rotation axis and the equator after the first reflection of torsional waves at the boundaries [examples of these are labelled as (c'), (e) and (f)]. We note that this effect is particularly prominent near the rotation axis, where the gradient of the magnetic field profile is steep. One explanation for the observed wave patterns is that strong magnetic field gradients cause continual reflections of propagating waves in the narrow region of the core between $s = 0$ and $s \approx 500\,\mathrm{km}$, resulting in waves becoming partially trapped within this region.
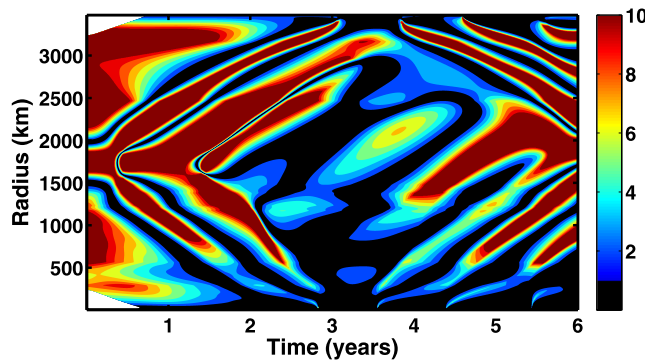
Figure 14. Contour plots of α, as defined by eq. (20), over one complete transit time (6 yr) in the full sphere model with varying $\{B_s^2\}$. Black regions ($\alpha < 1$) are locally 'dispersive', since term 1 is smaller than at least one of the other terms. Coloured regions are locally 'non-dispersive', with the magnitude of term 1 at least equal to that of the other terms in the blue regions and exceeding the other terms by at least a factor of 10 in the red regions. White regions show areas where the terms are very small and calculating the ratio would therefore be numerically intractable.

3.4 Local wave speed

Dumberry (2009) investigated dispersion of torsional normal modes by substituting solutions of the following form into the torsional wave equation

$$u_\phi = U_0 e^{-i\omega t + iks},$$

where ω is the angular frequency and k is the wavenumber. For large k values, the second spatial derivative (k^2 for the above form of solution) dominates the other terms on the RHS of the wave equation and we obtain

$$\omega^2 = \frac{\{B_s^2\}}{\mu_0 \rho_0} k^2,$$

from which the Alfvén wave group velocity

$$V_A = \frac{\partial \omega}{\partial k} = \sqrt{\frac{\{B_s^2\}}{\mu_0 \rho_0}} \tag{21}$$

may be recovered. In models (i) and (ii) of travelling torsional waves, results of which are shown in Figs 3 and 5, the cylindrical average of the radial magnetic field, $\{B_s^2\}$ was kept to a constant 4 (mT)^2. From the above Alfvén wave group velocity, it is possible to compare the theoretically predicted local wave speeds with those obtained in the models. Substituting the constants used in the models into eq. (21) results in a predicted local wave speed of $\sim 0.018\,\mathrm{m\,s^{-1}}$. Using the gradient of the wave travel path in our model results (the time taken for the pulse to traverse a particular distance), we obtain a local wave speed of $\sim 0.018\,\mathrm{m\,s^{-1}}$ as predicted. This group velocity was used to calculate the theoretical reflection time from the boundaries and used to produce Figs 8 and 9, which show the wave velocity profiles 1 yr before and after reflection.

In the results of model (iii), we observed all of the geometric effects observed in previous models with constant $\{B_s^2\}$ profiles, which included angular momentum effects, trailing wakes left behind wave pulses, geometric dispersion and phase shifts at the boundaries. In addition to these geometric effects, we also observed several features that arise due to magnetic field variations such as curved pulse travel paths, an internal reflection from the global field maximum and partially trapped waves near the boundaries. The trajectories of the pulses are curved due to variations in local Alfvén group velocity; we checked the local group velocity at several points during wave propagation by comparing the travel path gradients in the velocity contour plot (Fig. 12) with the predicted V_A according to eq. (21), and found that the calculated and predicted values were in agreement.

4 DISCUSSION AND CONCLUSIONS

We set out to investigate the effects of core geometry and geometric dispersion on the propagation of torsional waves. Using the AB3 method, we produced 1-D forward models of torsional waves (i) in a full sphere and (ii) in an equatorially symmetric spherical shell with constant $\{B_s^2\}$ and (iii) in a full sphere with a spatially varying $\{B_s^2\}$ profile. We have shown how waves propagate through the domains and how their local properties change both during propagation and during interactions with the boundaries at $s = 0$ and $s = r_c$. In this section, we elaborate on the results presented in Section 3.

4.1 The failure of Huygens' principle and dispersion in 2-D

The general wave equation for a scalar f is

$$\frac{\partial^2 f}{\partial t^2} = c^2 \nabla^2 f, \tag{22}$$

where c^2 is the wave group speed.

In Section 3, we commented upon the existence of dispersion and trailing wakes behind the wave pulses in our models. For the general wave equation above, the latter feature is related to what is termed the failure of Huygens' minor premise in even spatial dimensions. Huygens' minor premise states that a wave disturbance is localized in space and time (Hadamard 1923, pp. 53). For example, a wave packet arriving at an initially quiescent location would depart after a finite time period leaving a quiescent state. This premise is known to hold for symmetric waves obeying eq. (22) in odd spatial dimensions; for example, waves in 1-D are characterized by the solution (16), which has this property, as does the equivalent formula for spherically symmetric waves in 3-D

$$u = \frac{1}{r} \left[F_+(r + ct) + F_-(r - ct) \right], \tag{23}$$

where r is the spherical radius. However, it has been shown [Courant & Hilbert (1962, pp. 765–766); Hadamard (1923, pp. 53, 176–177)] that Huygens' minor premise fails in even dimensions and behind any wave pulse will be an infinite reverberation. Eq. (22) can be written in cylindrical coordinates as

$$\frac{\partial^2 f}{\partial t^2} = c^2 \left(\frac{\partial^2 f}{\partial s^2} + \frac{1}{s} \frac{\partial f}{\partial s} \right), \tag{24}$$

and the second term on the RHS is linked to the failure of Huygens' principle in this geometric setting. Although torsional waves may be modelled in 1-D, 2-D or 3-D, we believe that they are fundamentally a 2-D phenomenon due to their convergence on an axis at $s = 0$. This convergence imposes many conditions on the velocity and its derivatives, and changes the shape of wave pulses due to phase shifts (see Section 4.2). The torsional wave equation differs from the general cylindrically symmetric wave equation for a scalar, eq. (24), for several reasons. First, torsional waves are Alfvénic, meaning that the local wave group speed depends on the strength of the magnetic field at a particular location. This is taken into account by terms 6 and 7 on the RHS of eq. (19). Second, the height of the geostrophic cylinders changes due to the spherical boundary of the CMB, which gives rise to terms 3 and 4 in eqs (17) and (19). Finally, the velocity $\boldsymbol{u}$ is a vector field, of which torsional waves involve only the azimuthal component u_ϕ. Term 5 of eqs (17) and (19) arises due to the vector nature of the velocity field. As term 2 on the RHS of the torsional wave equation (eqs 17 and 19) is the same as the term linked to the failure of Huygens' principle for the general wave eq. (24), it is of interest to investigate where in the domain this term is large and whether these regions correspond to where trailing wakes are observed in our models. In order to do this, we produced individual contour plots of the ratio of term 1 to terms 2–5 on the RHS of eq. (17) during one core transit time (6 yr). These plots, found in Appendix B (Figs B1 a–d), have the same colour scale as figures 10 and 14.

Dispersion is observed in our torsional wave models as trailing wakes in the centre of the domain and as energy spreading out in the regions close to $s = 0$ and $s = r_c$ after a wave has passed through. From Figs B1(a–d), it seems that dispersion arises in our models due to the dominance of different terms in different regions of the domain. Terms 2 and 5 are large near to the rotation axis, while terms 3 and 4 are large near to the equator of the CMB. This suggests that all of these terms are sources of dispersion near the boundaries of the model domain. The regions in which term 2 is dominant, shown in Fig. B1(a), correspond to the regions in the centre of the domain where we observe trailing wakes in our models. Since the other terms on the RHS of eq. 17 are smaller than term 2 in the same regions at those times, we conclude that the failure of Huygens' principle in the geometric setting of torsional waves is related to the observed trailing wakes, and is therefore a source of dispersion in our models.

4.2 Phase shift at the boundaries

In this section, we explain the change in wave profile upon reflection at the boundaries, which was reported in Section 3.1 and Figs 8 and 9. The reader is reminded that the rotation axis is not a physical boundary, but a singular point of the coordinate system at which an infinite set of constraints is satisfied, and as such, an explanation of the observed pseudo-reflection is not trivial. Morse & Feshbach (1953) investigated transient (wave) motion on a circular membrane of radius $r = a$ and, by considering normal modes, found that a wave undergoes a $\pi/4$ phase shift when traversing the region $r \approx 0$ to $r \approx a$. In Appendix A, we perform a similar analysis to that detailed in Morse & Feshbach (1953) for torsional normal modes, whose analytic form is known in a cylindrical container (constant z_T), and show that phase shifts can explain the observed wave behaviour. We also investigate the possibility of torsional waves undergoing a Hilbert transform at the rotation axis, a phenomenon that was first reported by Powell (1994) for waves passing through the focal point of a circular membrane. From these analyses, we conclude that while some narrow initial pulses appear to undergo a uniform phase shift at the rotation axis, in general, an arbitrary initial pulse will undergo a more complicated phase shift that cannot readily be understood as a Hilbert transform.

4.3 Implications for torsional waves in the Earth's core

In the Earth's interior, the inner core is thought to have strong electromagnetic coupling with the outer core, which was not included in our models. In that case, one would expect the core fluid above and below the inner core (regions II and III in Fig. 1b) to rotate rigidly inside the tangent cylinder at the same speed as the inner core. Electromagnetic coupling to the inner core would quickly dissipate torsional waves entering the tangent cylinder and, consequently, waves would not exist long enough to reflect from the rotation axis and reenter the outer core as they do in our models. The reflection at the tangent cylinder observed in Fig. 7 is an interesting feature that may have implications for torsional waves in the geophysical context. If a torsional wave were generated outside the tangent cylinder in the Earth's core by a local impulse in space and time, as opposed to a temporally periodic global forcing, we could only expect to observe the outwards travelling pulse once at the CMB before it is reflected back into the core and absorbed on the tangent cylinder. However, as the discontinuity in the derivative of the cylinder height causes waves to be partially reflected at the tangent cylinder, it is possible that they could be observed at the CMB at regular intervals and may then be linked with decade variations in SV and/or ΔLOD. Another possible source of internal reflections of torsional waves in the Earth's core are strong gradients in the radial magnetic field, as seen in Fig. 12 (pulse B). However, the reflection coefficients for pulses A and B are both very small and it is possible that these internally reflected pulses would immediately be damped or dispersed upon reaching the CMB such that regular observation is impossible.

The analysis by Dumberry (2009) reproduced in Section 3.4 implies that short wavelength torsional normal modes, corresponding to high wavenumbers, are non-dispersive. Our findings are consistent with that conclusion because we find that, for travelling torsional waves, narrow (short wavelength) wave profiles are less dispersive than wider pulses (see Fig. 11). This result may be particularly important when studying torsional waves in the Earth's core because those inferred from SV data appear to be relatively long wavelength. For example, the smallest features of torsional waves presented in Gillet *et al.* (2010) occupy approximately one-fifth of the core radius and those presented in Hide *et al.* (2000) occupy almost the entire core radius. Our analyses of dispersive regions and the evolution of our modelled waves suggest

that torsional waves in the core may undergo a significant dispersion process that arises solely as a result of core geometry. This geometric dispersion is an effect that has previously been neglected in torsional wave studies. Recent work by Schaeffer *et al.* (2012) discusses Alfvén wave reflection properties and energy dissipation in boundary layers based on the ratio of kinematic viscosity to magnetic diffusion (the magnetic Prandtl number, P_m). They argue that for geophysically relevant liquid metals, corresponding to $P_m \ll 1$, little energy is dissipated during a single reflection at $s = r_c$ but that many successive reflections may lead to significant dissipation. Dissipative processes are damping mechanisms for waves; they dissipate wave energy and decrease wave amplitude. Schaeffer *et al.* (2012) define a quality factor for reflected waves and conclude that torsional wave normal modes could survive in the Earth's core for a few periods of the fundamental modes, which they take as 6 yr. Given that successive reflections from the boundaries significantly changes the shape of wave pulses in our models, as seen in Figs 3, 4 and 5, we suggest that terrestrial torsional waves would undergo significant dispersion (energy spreading) irrespective of, and in addition to, any dissipative (damping) effects and therefore may not survive as distinct pulses for several transits of the Earth's core.

ACKNOWLEDGEMENTS

REFERENCES

Abramowitz, M. & Stegun, I.A., 1984. *Pocketbook of Mathematical Functions,* Verlag Harri Deutsch.

Backus, G., 1968. Kinematics of geomagnetic secular variation in a perfectly conducting core, *Phil. Trans. R. Soc. Lond., A,* **263,** 239–266.

Braginsky, S.I., 1970. Torsional magnetohydrodynamic vibrations in the Earth's core and variations in the length of day, *Geomagn. Aeron.,* **10,** 1–10.

Braginsky, S.I., 1984. Short-period geomagnetic secular variation, *Geophys. astrophys. Fluid Dyn.,* **30,** 1–78.

Buffett, B.A., 2010. Tidal dissipation and the strength of the Earth's internal magnetic field, *Nature,* **468,** 952–954.

Buffett, B.A., Mound, J. & Jackson, A., 2009. Inversion of torsional oscillations for the structure and dynamics of Earth's core, *Geophys. J. Int.,* **177,** 878–890.

Bullard, E.C. & Gellman, H., 1954. Homogeneous dynamos and terrestrial magnetism, *Phil. Trans. R. Soc. Lond., A,* **247,** 213–278.

Canet, E., Fournier, A. & Jault, D., 2009. Forward and adjoint quasi-geostrophic models of the geomagnetic secular variation, *J. geophys. Res.,* **114,** B11101, doi:10.1029/2008JB006189.

Christensen, U. & Wicht, J., 2007. Numerical dynamo simulations, in *Treatise on Geophysics,* Vol. 8, pp. 245–279, ed. Olson, P., Elsevier.

Courant, R. & Hilbert, D., 1962. *Methods of Mathematical Physics,* Vol. II, Wiley.

Dumberry, M., 2009. Taylor's constraint and torsional oscillations, in *Les Houches,* Session LXXXVIII: Dynamos, pp. 383–401, eds Cardin, P. & Cugliandolo, L.F., Elsevier.

Dumberry, M. & Bloxham, J., 2003. Torque balance, Taylor's constraint and torsional oscillations in a numerical model of the geodynamo, *Phys. Earth planet. Inter.,* **140**(1–3), 29–51.

Durran, D.R., 1991. The third-order Adams-Bashforth method: an attractive alternative to leapfrog time differencing, *Mon. Weather Rev.,* **119**(3), 702–720.

Gillet, N., Jault, D., Canet, E. & Fournier, A., 2010. Fast torsional waves and strong magnetic field within the Earth's core, *Nature,* **465**(74), 74–77.

Glatzmaier, G.A. & Roberts, P.H., 1995. A three-dimensional self-consistent computer simulation of a geomagnetic field reversal, *Nature,* **377,** 203–209.

Hadamard, J., 1923. *Lectures on Cauchy's Problem in Linear Partial Differential Equations,* Yale Univ. Press.

Hide, R., Boggs, D.H. & Dickey, J.O., 2000. Angular momentum fluctuations within the Earth's liquid core and torsional oscillations of the core-mantle system, *Geophys. J. Int.,* **143,** 777–786.

Hollerbach, R., 1996. On the theory of the geodynamo, *Phys. Earth planet. Inter.,* **98,** 163–185.

Jackson, A., Bloxham, J. & Gubbins, D., 1993. Time-dependent flow at the core surface and conservation of angular momentum in the coupled core-mantle system, in *Dynamics of Earth's Deep Interior and Earth Rotation,* Geophysical Monograph, Vol. 72, pp. 97–107, AGU.

Jackson, A., Jonkers, A. R.T. & Walker, M.R., 2000. Four centuries of geomagnetic secular variation from historical records, *Phil. Trans. R. Soc. Lond., A,* **358,** 957–990.

Jault, D. & Légaut, G., 2005. Alfvén waves within the Earth's core, in *Fluid Dynamics and Dynamos in Astrophysics and Geophysics,* pp. 277–293, eds Soward, A.M., Jones, C.A., Hughes, D.H. & Weiss, N.O., The Fluid Mechanics of Astrophysics and Geophysics, CRC Press.

Jault, D., Gire, C. & LeMouël, J.L., 1988. Westward drift, core motions and exchanges of angular momentum between core and mantle, *Nature,* **333**(26), 353–356.

Kuang, W., 1999. Force balances and convective states in the Earth's core, *Phys. Earth planet. Inter.,* **116,** 65–79.

Kuang, W. & Bloxham, J., 1997. An Earth-like numerical dynamo model, *Nature,* **389,** 371–374.

Le Mouël, J.L., 1984. Outer-core geostrophic flow and secular variation of Earth's geomagnetic field, *Nature,* **311**(5988), 734–735.

Le Mouël, J.L., Gire, C. & Madden, T., 1985. Motions at core surface in the geostrophic approximation, *Phys. Earth planet. Inter.,* **39,** 270–287.

Légaut, G., 2005. Ondes de torsion dans le noyau terrestre, *PhD thesis,* Observatoire de Grenoble, Laboratoire de Geophysique Interne et Tectonophysique.

Lewis, H.R. & Bellan, P.M., 1990. Physical constraints on the coefficients of Fourier expansions in cylindrical coordinates, *J. Math. Phys.,* **31**(11), 2592–2596.

Livermore, P.W. & Hollerbach, R., 2012. Successive elimination of shear layers by a hierarchy of constraints in inviscid spherical-shell flows, *J. Math. Phys.,* **53**(7), 073104, http://dx.doi.org/10.1063/1.4736990.

Livermore, P.W., Hollerbach, R. & Jackson, A., 2013. Electromagnetically driven westward drift and inner-core superrotation in Earth's core, *Proc. Natl. Acad. Sci. USA,* **110,** 15 914–15 918.

Morse, P. & Feshbach, H., 1953. *Methods of Theoretical Physics,* Vol. 1, McGraw-Hill.

Mound, J. & Buffett, B., 2007. Viscosity of the Earth's fluid core and torsional oscillations, *J. geophys. Res.,* **112,** B05402, doi:10.1029/2006JB004426.

Pais, A. & Hulot, G., 2000. Length of day decade variations, torsional oscillations and inner core superrotation: evidence from recovered core surface zonal flows, *Phys. Earth planet. Inter.,* **118,** 291–316.

Powell, A., 1994. The focal phase shift of waves of a circular membrane, applied to underexpanded supersonic jet structure, *J. acoust. Soc. Am.,* **97**(2), 927–932.

Roberts, P., 2007. Theory of the Geodynamo, in *Treatise on Geophysics,* pp. 67–105, ed. Schubert, G., Elsevier.

Roberts, P.H. & Aurnou, J.M., 2011. On the theory of core-mantle coupling, *Geophys. astrophys. Fluid Dyn.,* **106**(2), 157–230.

Rotvig, J. & Jones, C., 2002. Rotating convection-driven dynamos and low Ekman number, *Phys. Rev. E,* **66**, 056308, doi:10.1103/PhysRevE.66.056308.

Schaeffer, N., Jault, D., Cardin, P. & Drouard, M., 2012. On the reflection of Alfvèn waves and its implication for Earth's core modelling, *Geophys. J. Int.,* **191**(2), 508–516.

Shearer, P., 2009. *Introduction to Seismology,* 2nd edn, Cambridge Univ. Press.

Stellmach, S. & Hansen, U., 2004. Cartesian convection driven dynamos at low Ekman numbers, *Phys. Rev. E,* **70**, 056312, doi:10.1103/PhysRevE.70.056312.

Takahashi, F., Matsushima, M. & Honkura, Y., 2005. Simulations of a quasi-Taylor state geomagnetic field including polarity reversals on the Earth simulator, *Science,* **309**, 459–461.

Taylor, J.B., 1963. The magneto-hydrodynamics of a rotating fluid and the Earth's dynamo problem, *Proc. R. Soc. Lond., A,* **9**, 274–283.

Teed, R.J., Jones, C.A. & Tobias, S.M., 2013. The dynamics and excitation of torsional waves in geodynamo simulations, arXiv:1307.6048.

Wicht, J. & Christensen, U.R., 2010. Torsional oscillations in dynamo simulations, *Geophys. J. Int.,* **181**, 1367–1380.

Zatman, S. & Bloxham, J., 1997. Torsional oscillations and the magnetic field within the Earth's core, *Nature,* **388**, 760–763.

Zatman, S. & Bloxham, J., 1999. On the dynamical implications of models of Bs in the Earth's core, *Geophys. J. Int.,* **138**(3), 679–686.

APPENDIX A: PHASE SHIFTS OF TORSIONAL WAVES IN A CYLINDER

For the purposes of the following discussion, we restrict ourselves to a simplified geometry consisting of a cylinder of radius 1, with constant $\{B_s^2\}$ such that the wave speed is 1. In this geometry, the general solution to the axisymmetric torsional wave equation is

$$u_\phi(s, t) = \sum_{j=1}^{\infty} N_j J_1(k_j s) \cos(k_j t), \tag{A1}$$

where N_j are coefficients determined by the initial condition, J_1 is the first-order Bessel function of the first kind and k_j is the jth zero of J_1 (e.g. Mound & Buffett 2007). These solutions satisfy the required regularity condition at the rotation axis and a no-slip condition ($u_\phi = 0$) at the outer boundary, rather than the stress-free condition that has previously been considered in this work. For large argument, $k_j s$, the asymptotic behaviour of J_1 is

$$J_1(k_j s) \approx \sqrt{\frac{2}{\pi k_j s}} \cos\left(k_j s - \frac{3\pi}{4}\right), \tag{A2}$$

for example, Abramowitz & Stegun (1984). Substitution of (A2) into eq. (A1) gives the following general solution away from the rotation axis

$$u_\phi(s, t) \approx \frac{1}{2} \sum_{j=1}^{\infty} N_j \sqrt{\frac{2}{\pi k_j s}} \left\{ \cos\left[k_j(s - t) - \frac{3\pi}{4}\right] + \cos\left[k_j(s + t) - \frac{3\pi}{4}\right] \right\}, \tag{A3}$$

which represents two waves travelling in opposite directions. Assuming an initial Gaussian wave profile centred at $s = 1/2$, the wave travelling towards the rotation axis (the 'incoming' wave) at time $t = 0$ is

$$u_\phi(s, 0) \approx \frac{1}{2} \sum_{j=1}^{\infty} N_j \sqrt{\frac{2}{\pi k_j s}} \cos\left(k_j s - \frac{3\pi}{4}\right). \tag{A4}$$

At time $t = 1$, this incoming wave packet has reflected at the rotation axis and is again centred at $s = 1/2$ and travelling outwards towards $s = 1$. The outgoing wave profile is

$$u_\phi(s, 1) \approx \frac{1}{2} \sum_{j=1}^{\infty} N_j \sqrt{\frac{2}{\pi k_j s}} \cos\left[k_j(s - 1) - \frac{3\pi}{4}\right], \tag{A5}$$

which has undergone a phase shift of $-k_j$ in each mode with respect to the incoming wave. Using the asymptotic expansion of J_1 given by eq. (A2), we find an expression for the zeroes

$$k_j \approx \frac{3\pi}{4} + \left(j - \frac{1}{2}\right)\pi, \tag{A6}$$

which implies the following index-dependent phase shift at the rotation axis

$$\psi = \begin{cases} \frac{\pi}{4} & j \text{ even,} \\ -\frac{3\pi}{4} & j \text{ odd.} \end{cases} \tag{A7}$$

Note that at time $t = 0$, both the incoming and outgoing waves are described by eq. (A4). Wave behaviour at the outer boundary, $s = 1$, is considered by comparing the initial outgoing wave with the incoming wave profile at time $t = 1$, which gives a phase shift of $+k_j$ in every mode.

(a)

(b)
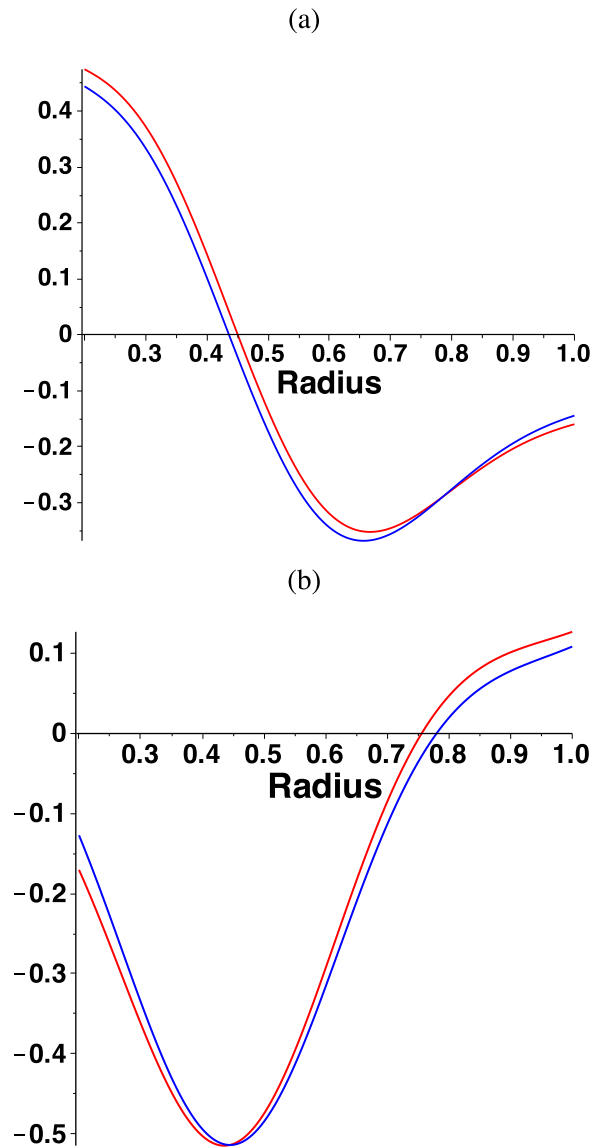
Figure A1. (a) Comparison of the outgoing wave in a cylinder of radius 1 at time $t = 1$ (after reflection at the rotation axis) according to the normal-mode solution given by eq. (A1) (blue line) and the phase shifted asymptotic approximation to the normal-mode solutions, given by eqs (A3) and (A7) (red line). (b) Comparison of the incoming wave in a cylinder of radius 1 at time $t = 1$ (after reflection at the outer boundary $s = 1$) according to the normal-mode solution given by eq. (A1) (blue line) and the phase shifted asymptotic approximation to the normal-mode solutions, given by eqs (A3) and (A7) (red line).

In the above analysis, we have used the asymptotic approximations to torsional normal modes in a cylinder to investigate the predicted phase shift at the rotation axis and at the outer boundary (for a no-slip boundary condition). These predicted phase shifts are not uniform, but depend on the mode under consideration. Since the normal-mode solutions to the torsional wave equation in a cylinder are known, it is of interest to compare these analytic solutions with the wave profiles approximated by their phase shifted asymptotic form, which is given by eqs (A3) and (A7). The initial wave profile described by eq. (12), with $\sigma = 0.1$, was projected onto the first 20 normal modes of the system and evolved through time. Figs A1(a) and (b) show, respectively, the travelling wave solution given by the normal-mode projections (blue line) and their phase shifted asymptotic form (red line) for reflections at $s = 0$ and $s = 1$. In both cases, the two wave profiles are very similar, which indicates that the reflections are adequately described by the k_j (index-dependent) phase shift of the asymptotic approximations. Interestingly, the index-dependent phase shifts reproduce the analytic normal-mode wave behaviour for both the rotation axis and $s = 1$, despite the former being a singular point and the latter a physical boundary.

Powell (1994) investigated the phase shift of waves on a circular membrane when passing through, or reflecting from, the focal point. By considering normal modes and their periodic approximations, he found that the divergent (outgoing) waveform is found by phase shifting the convergent (incoming) waveform by $-\pi/2$ in every mode. As a uniform $\pi/2$ phase shift of a waveform constitutes its Hilbert transform
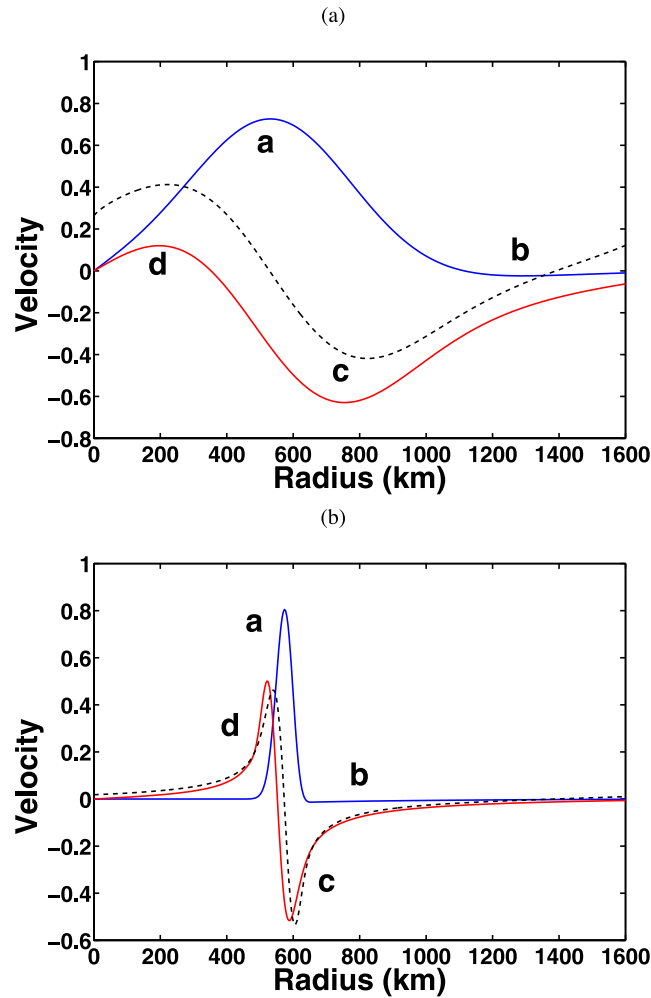
Figure A2. (a) Velocity profiles of the waves 1 yr before (blue) and after (red) reflection at the rotation axis in the full sphere model (i). The annotations correspond to those in Fig. 3 and the times at which the profiles were taken are shown in that figure as two vertical black lines. The black dashed line is the Hilbert transform of the incoming wave (the blue line). Note that the Hilbert transform is somewhat similar to the outgoing wave (the red line). (b) Velocity profiles of the waves 1 yr before (blue) and after (red) reflection at the rotation axis in a full sphere model with a narrow initial profile ($\sigma = 0.01$). The black dashed line is the Hilbert transform of the incoming wave (the blue line). Note the increased similarity of the Hilbert transform to the outgoing wave (the red line).

[the sign of the phase shift depends on the convention, e.g. Shearer (2009, p. 155)], Powell (1994) concluded that the focal shift of waves on a circular membrane is equivalent to the Hilbert transform of the converging wave. For narrower initial profiles than those shown in Figs A1(a) and (b), which used $\sigma = 0.1$, we recover this result for our normal-mode projections. Although the normal-mode projections and their phase shifted asymptotic approximations remain very similar, the outgoing wave after reflection at the rotation axis also strongly resembles the Hilbert transform of the incoming wave profile, which in this case, converts the cosines in eq. (A3) to sines. It seems that, for a sufficiently narrow pulse, the overall wave behaviour of the predicted phase shift, for which some normal modes are shifted by $\pi/4$ and others by $-3\pi/4$, averages to mimic the behaviour of a uniform $\pi/2$ phase shift.

We might expect to recover a similar result in our torsional wave models because the region near to the rotation axis in a spherical geometry is well-approximated by a cylinder (constant z_T). For our torsional wave models, which are in a full sphere and an equatorially symmetric spherical shell, there is empirical evidence to suggest that the Hilbert transform is recovered for narrow pulses after reflection at the rotation axis. Fig. A2(a) shows the wave profiles 1 yr before (blue line) and after reflection (red line) in the previously discussed full sphere model (i), with the Hilbert transform of the blue profile drawn in black. For this initial profile, with $\sigma = 0.1$, we see that although the general shape of the Hilbert transform matches the reflected wave profile, the required regularity condition is not met at rotation axis, which implies that the wave has undergone a more complex reflection than a uniform $\pi/2$ phase shift. However, when the initial profile is much narrower, as shown in Fig. A2(b) for $\sigma = 0.01$, the shape of the Hilbert transform and reflected wave profile match more closely and the Hilbert transform better matches the regularity condition at $s = 0$.

APPENDIX B: DISPERSION FIGURES

(a)

(b)

(c)

(d)
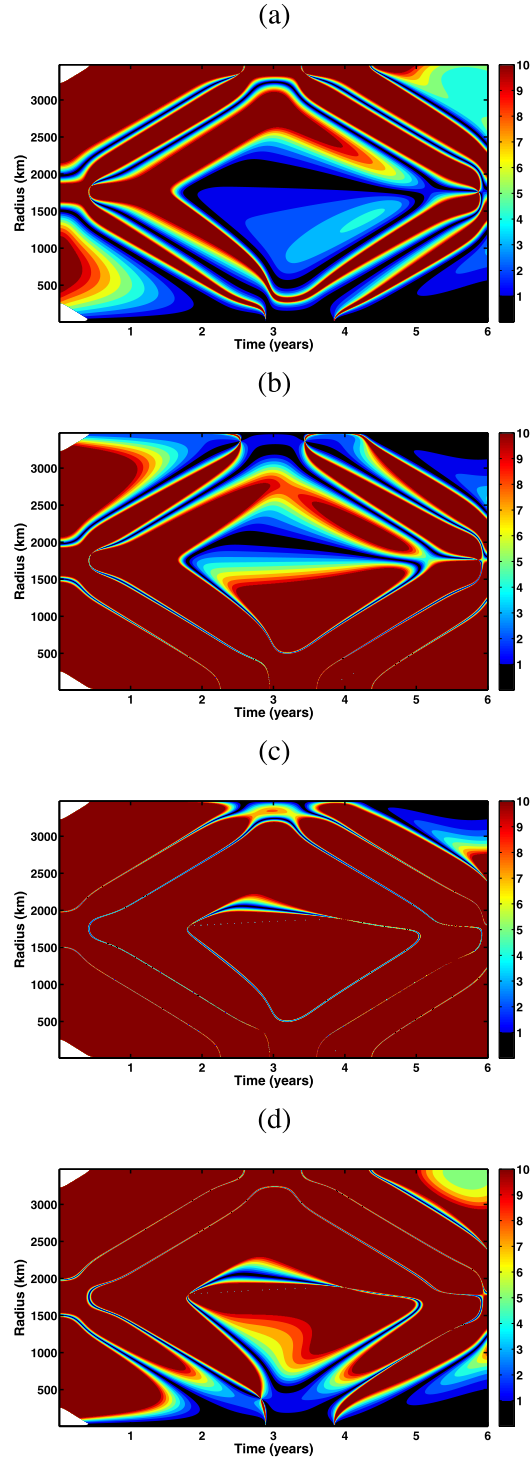
Figure B1. Contour plots of the magnitude of the ratio of term 1 to (a) term 2 (b) term 3 (c) term 4 and (d) term 5, from the RHS of eq. (17), over one complete transit time (6 yr) in the full sphere model. Black regions are locally 'dispersive', since the relevant term is larger than term 1. Coloured regions are locally 'non-dispersive', with the magnitude of term 1 at least equalling that of the other term in the blue regions and exceeding the other term by at least a factor of 10 in the red regions. White regions show areas where the terms are very small and calculating the ratio would therefore be numerically intractable.